Role of mineralogical, structural and hydrodynamic rock properties in conduits formation in three distinct carbonate rock types

M Leger, L Luquot, Delphine Roubinet

Role of mineralogical, structural and hydrodynamic rock properties in conduits formation in three distinct carbonate rock types

M. Leger, L. Luquot and D. Roubinet

Abstract

Adopting sustainable strategies to manage water resources of karst reservoirs requires to understand the carbonate rock reactivity that is responsible for the formation of these reservoirs, as well as the role of the rock mineralogy in the conduit formation. To this end, three carbonate rocks (chalk, crinoidal limestone and dolomite) with different mineralogy and internal structure are submitted to laboratory dissolution experiments by injecting an acid solution under atmospheric conditions and various hydrodynamic conditions with a homemade experimental device. The core samples are characterized by petrophysical investigations with laboratory and imagery techniques before and after the experiments, and the changes in chemical and hydraulic properties are recorded during the experiment. The resulting carbonate dissolution leads to the formation of preferential conduits and the increase in porosity and permeability of the samples. For the three rock types, the dissolution rate mainly depends on the mineral composition, the flow conditions and the initial structural properties. In addition, we observe that (i) for each rock type, the lower Péclet conditions applied to the samples, the lower global dissolu-

tion rate, (ii) for each hydrodynamic condition, chalk and crinoidal limestone have the highest and smallest dissolution rates, respectively, (iii) for a similar amount of injected acid, the dissolution is lower in dolomite than in calcite, and (iv) high rock heterogeneities in the chalk samples are responsible for high renewal rates that induce high dissolution rates.

Keywords

Carbonate rock, Reactive transport, Dissolution rate, Micro-tomography, Karst, Wormholes

1. Introduction

The reactivity of carbonate rocks in natural or anthropogenic environment is a well-known fact in the scientific community. Nevertheless, there are still a lot of questions about this reaction process whereas its understanding is particularly essential as carbonate rocks reservoirs play an important role in human development. They are often used for water, oil or gas extraction, as well as for geothermal energy production or CO_2 sequestration (Rege and Fogler, 1989; Chilingarian et al., 1992; Noiriel et al., 2005; Moore and Wade, 2013; Akono et al., 2019).

Carbonate rocks display very heterogeneous media due to their high mineralogy variety and the high complexity of their structural properties over scales (Choquette and Pray, 1970; Lucia, 1983; Lønøy, 2006). A thermodynamic disequilibrium between a fluid and this medium is responsible for dissolution and karst formation for instance (Ford and Williams, 2007). In order to better understand dissolution processes inside carbonate rocks, laboratory experiments and numerical simulations are conducted under variable

conditions on different carbonate rock types. The two adimensional numbers Péclet (Pe) and Damköhler (Da) are generally used to link the initial conditions of experiments and the resulting dissolution patterns inside the rock (Golfier et al., 2002). The Péclet number defines the dominant mechanism, between advection and diffusion, for transport processes occurring inside the rock, whereas the Damköhler number characterizes the importance of this transport compared to reaction (Lasaga, 1984; de Marsily, 1986; Daccord et al., 1993). They are both dependent on the velocity at which the reactive fluid passes through the system, and on the characteristic length of it. Different experimental conditions are then related to different dissolution patterns, going from uniform dissolution to compact wormholes. The properties of the fluid injected inside the rock are shown as the most decisive factors in the development of dissolution regimes in a lot of experimental and numerical studies (Fredd and Fogler, 1998; Golfier et al., 2002; Noiriel et al., 2004; Luquot and Gouze, 2009; Smith et al., 2013; Vialle et al., 2014; Menke et al., 2015; Rohmer et al., 2016; Lebedev et al., 2017; Akono et al., 2019). In order to better understand the impact of the dissolution process on the rock, laboratory dissolution experiments are usually conducted on samples where the rock properties were initially characterized by laboratory measurements and/or from 3D-images calculations. Acidic fluid is then injected at various concentrations and flow rates in the samples. The evolution of rock properties, such as porosity, permeability, structural and mechanical properties, is monitored during the experiments. The effects of dissolution on limestone at room and reservoir conditions were studied (Fredd and Fogler, 1998; Noiriel et al., 2004; Luquot and Gouze, 2009; Noiriel et al., 2009; Vialle and Vanorio,

2011; Gharbi et al., 2013; Mangane et al., 2013; Vialle et al., 2014; Steefel et al., 2015; Lebedev et al., 2017; Akono et al., 2019), as well as the ones on dolomite, preferentially at reservoir conditions (Smith et al., 2013; Luhmann et al., 2014; Tutolo et al., 2014; Wang et al., 2021). Few studies analyze the role of the rock mineralogy or the initial internal rock structure, or concentrate on more complex rocks with pluri-minerals rock composition. Some studies showed that a heterogeneous pore size or pore shape distribution will affect the dissolution mechanisms and lead to different dissolution patterns inside the rock (Hoefner and Fogler, 1988; Noiriel et al., 2005; Vialle et al., 2013; Luquot et al., 2014; Wang et al., 2021). Others defined new dissolution patterns associated with internal rock structure (Menke et al., 2017). Recently, we demonstrated that local heterogeneities have a stronger control on dissolution localization than Pe and Da conditions (Leger et al., 2022). At large scale, large structural heterogeneities such as fractures impact the dissolution rate and shape since the dissolution preferentially takes place along these large heterogeneities, leading to dissolution mechanisms controlled by transport (Elkhoury et al., 2013; Garcia-Rios et al., 2017).

By studying dissolution patterns on different carbonate types in similar conditions, some studies partially tried to establish the role of local structural properties and mineral composition compared to flow and chemical boundary conditions. Sandstone and limestone show specific responses to dissolution (Rohmer et al., 2016). Silicates inside sandstone favoring dissolution due to non-reactive grains inside silicates, which leads to a larger reaction surface and then a higher dissolution rate and a more homogeneous dissolution (Garcia-Rios et al., 2017). Additionally, structural properties inside these

two rock types are responsible for different dissolution patterns at local scale inside the studied samples (Vialle et al., 2013). It has been demonstrated that textural differences inside various fractured limestone rock types influence dissolution patterns but do not have a significant impact on dissolution rates (Levenson et al., 2015). These studies do not allow seeing the impact of mineralogy differences in the dissolution of carbonate rock types.

In order to acquire further insights on this matter, the present study predominantly focuses on the differences in dissolution patterns depending on the mineralogy and on the structure of different carbonate rock types, as well as on the experimental hydrodynamic conditions. To this end, three distinct carbonate rock types are selected for their differences in structure and mineralogy: chalk, crinoidal limestone and dolomite. Acid injections are conducted on samples cored from these three rock types at atmospheric conditions. With the same acidic fluid, four Péclet conditions, associated to different flow rates depending on the rock type, were applied to the samples with a homemade experimental device. Samples are characterized with laboratory and images methods before and after these experiments, during which chemical and hydraulic properties are recorded. The rock properties evolution, associated with the initial structural and mineral differences between the three rock types and the experimental conditions, is analyzed in order to determine the influence of each of these parameters on the dissolution patterns induced by the acid injection into the rocks. The discussion of this study will focus on the role of initial properties until the conduits formation.

2. Materials and Methods

The studied rock samples and the full experimental protocol used here are presented in details in Leger and Luquot (2021) and Leger et al. (2022), and the key parts of the experimental protocol are reminded in Supplementary Material. In this section, basic information are provided in order to understand the methodology and the obtained results.

2.1. Rock properties and characterization

The eleven cores samples studied are part of three different carbonate types. They were cored in three rock blocks in the same orientation in cores of 20-30 mm length and 18 mm diameter, surrounded with epoxy resin and PVC pipe for a total diameter of 25 mm, i.e., one inch. Four samples come from a chalk cave near Le Havre, Normandie, north-western France, and are characterized by flint chalk from the lower Senonian. This group of samples is named *Normandie* and the samples labels are N03, N05, N08 and N09. A set of five samples was cored into a limestone block from Euville quarry near Nancy, north-eastern France, and is defined as crinoidal limestone from the Oxfordian. It is called *Euville* and the cores are named E01, E02, E04, E05 and E08. The two last samples were cored in the Lexos quarry near Toulouse, south-western France, described as a reddish recrystallized limestone from the Bajocian lately dolomitized. The set of samples is named *Lexos* with samples L01 and L04.

X-ray Diffraction (XRD) on a Bruker D8 Discover, X-ray Fluorescence (XRF) measurements and Scanning Electron Microscopy (SEM) on a FEI Quanta 200 FEG observations show that Normandie and Euville rocks are fully composed of calcite ($CaCO_3$), whereas Lexos is made up of dolomite

115 ($CaMg(CO_3)_2$). The dolomite formula is determined using the Ca and Mg
116 outlet concentrations during the percolation experiments assuming that the
117 dissolution is stoechiometric and no precipitation reaction occurs from the
118 dissolution. For the two experiments on dolomite, constant $\frac{Ca}{Mg}$ ratio is ob-
119 served at the outlet and the dolomite formula is established to be $Ca_{1.06}Mg_{0.94}(CO_3)_2$.
120 Scanning Electron Microscopy (SEM) and 3D X-ray micro-tomography (XRMT)
121 display images where structural differences between the three rocks are shown,
122 especially in pores size and shape. As it can be seen in Figure 1, Euville dis-
123 plays the largest pores followed by Lexos and then Normandie.

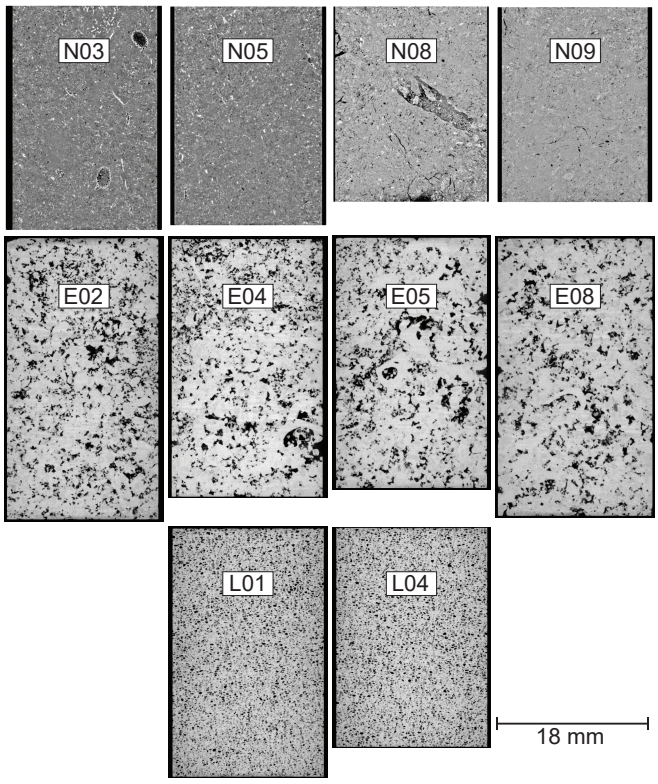

Figure 1: 2D vertical slices from 3D X-ray micro-tomography (XRMT) images of the initial structure of all the samples from the three rock types.

To characterize the cores samples, petrophysical measurements were done by non-destructive laboratory methods. Porosity, permeability and velocities of P and S waves are carried out on dry and/or saturated samples. Current injection inside the saturated samples gives the rock conductivity and allows to calculate structural properties from Archie's law (Archie, 1942), such as the formation factor F, cementation index m and electrical tortuosity τ_e. Characterization of pore size distribution between 0.5 and 140 μm is carried out by centrifugation. XRMT images are collected with a pixel size of 12 μm and are analyzed with a homemade software to obtain complementary information about the samples. The properties calculated from the 3D images are porosity, permeability, hydraulic tortuosity τ_h and relative pores size $\frac{S}{V}$. A pore size distribution is also obtained from a probabilistic method displaying chord lengths. Details on rock types, calculation methods and protocols, complete results and discussion on the samples properties are provided in Leger and Luquot (2021).

2.2. Experimental protocol

The experimental protocol described here is the same as the one used in Leger et al. (2022). Under atmospheric pressure and temperature conditions, acidic solution is injected through the samples. The injected solution is composed of water previously balanced with the different rock types, acetic acid CH_3COOH and sodium acetate CH_3COONa. The acid concentration is about 10^{-2} mol/L with a pH of 4. Figure 2 displays the homemade experimental device used for the percolation experiments. The acid solution is stored in a beaker where conductivity and pH are monitored continuously, and is injected through the core sample by a peristaltic pump. Sensors of

absolute and differential pressure continuously record the pressure difference between the sample inlet and outlet. At the device outlet, samplings of 5 mL are continuously carried out during day time and punctually during night time. pH, conductivity and cation concentrations are measured for each sampled fluid.

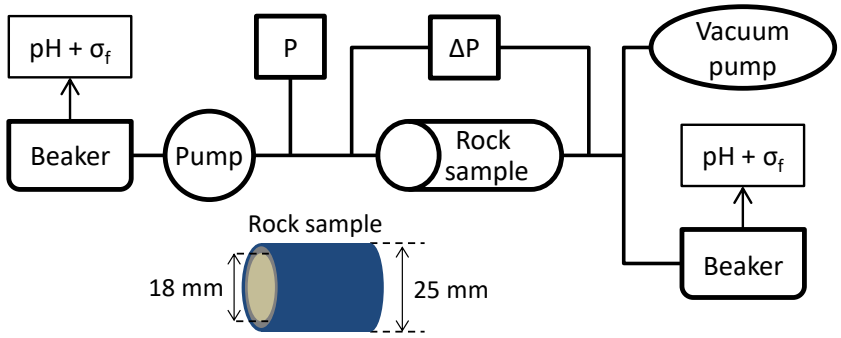

Figure 2: Top: Homemade experimental device used for the percolation experiments, with P the absolute pressure sensor and ΔP the differential pressure sensor. Bottom: Scheme of the cylindrical core rock sample fixed inside a PVC tube.

The aim of this study being to compare the behavior of three different rock types during percolation experiments, similar experimental conditions are applied to the samples from the different rock types. In order to evaluate the impact of the hydraulic conditions, four Péclet numbers (Pe_1, Pe_2, Pe_3 and Pe_4) are chosen and the corresponding flow rates are applied to the samples. Pe is defined as $Pe = \frac{ul}{d}$ with u the flow velocity injected in each sample [m/s], l the characteristic length of the pores [m] and d the molecular diffusion coefficient for fresh water at 25°C set to 5×10^{-9} m^2/s. The characteristic length l is based on the pore size distribution calculated in Leger and Luquot (2021) and is displayed in ranges that depend on the considered rock type. Therefore, average Pe values for each rock type are

resulting from these l ranges, and the average values between the three rock types are considered to simplify the description. Péclet numbers stand as $Pe_1 = 0.09$, $Pe_2 = 0.65$, $Pe_3 = 1.97$ and $Pe_4 = 5.26$.

The experimental conditions and the associated samples are summarized in Table 1. Note that the experiments conducted on the Normandie samples come from Leger et al. (2022). Reproduction experiments are conducted for Normandie and Euville with similar conditions for N03 and N08 on one side, and E01 and E02 on the other side. To simplify the results interpretation, the experiments conducted with the hydraulic conditions Pe_3 and Pe_4 will be discussed together in Sections 3 and 4.

	Normandie		Euville		Lexos	
Pe	Sample	Q	Sample	Q	Sample	Q
Pe_1	N09	8.0e-10	E08	9.3e-11		
Pe_2	N03 & N08	7.0e-9	E01 & E02	5.0e-10	L01	3.2e-9
Pe_3	N05	1.8e-8	E05	2.5e-9	L04	7.6e-9
Pe_4			E04	6.0e-9		

Table 1: Experimental transport conditions, Péclet numbers Pe [-] and flow rates Q [m^3/s], of the percolation experiments.

2.3. Experimental output

The measurement of pressure difference allows to calculate the evolution of the samples permeability k during the experiment using the Darcy law:

$$k = \frac{QL\mu}{A\Delta P}, \tag{1}$$

where Q is the flow rate [m^3/s], L the sample length [m], μ the dynamic viscosity of water [Pa.s] set to 0.001 Pa.s, A the surface of fluid injection [m^2]

and ΔP the differential pressure between the inlet and outlet of the sample [Pa].

Concentration of Ca ions for the three rock types and that of Mg for Lexos rock are measured by ICP-AES (Inductively Coupled Plasma Atomic Emission Spectroscopy, Cirad, Montpellier) in the outlet samplings collected at time t_i ($i = 1, ..., N$) with N the number of samples. The porosity is deduced from these concentrations based on the equivalence between the quantity of Ca or Ca Mg collected in the outlet fluid samples and the quantity of dissolved calcite or dolomite from the rocks, respectively. The calcium carbonate mass dissolved between times t_{i-1} and t_i, $m_{\mathrm{CaCO_{3t_i}}}$, is then expressed as

$$m_{\mathrm{CaCO_{3t_i}}} = \frac{([\mathrm{Ca}]_{t_i} - [\mathrm{Ca}]_{t_0})(t_i - t_{i-1})Q}{M_{\mathrm{Ca}}} M_{\mathrm{CaCO_3}} \tag{2}$$

with $[\mathrm{Ca}]_{t_i}$ the calcium concentration at the sampling time t_i [g/m^3], $[\mathrm{Ca}]_{t_0}$ the initial calcium concentration [g/m^3], $t_i - t_{i-1}$ the time spent since the last sampling [s], Q the flow rate [m^3/s], and M_{Ca} and $M_{\mathrm{CaCO_3}}$ the molecular masses of calcium and calcium carbonate, respectively [g/mol]. Concerning the dolomite rock type, the proportion of the mass of Ca and Mg from the dolomite formula $\mathrm{Ca_{1.06}Mg_{0.94}(CO_3)_2}$ allows to calculate $m_{\mathrm{CaMg(CO_3)_{2t_i}}}$. The equivalent volume of dissolved calcite and dolomite in the rock sample between each sampling step, V_{t_i}, is calculated by dividing m_{t_i} by the density of calcite and dolomite. Finally, the porosity ϕ_{t_i} is obtained from

$$\phi_{t_i} = \phi_{t_{i-1}} + \frac{V_{t_i}}{V_{ech}} \tag{3}$$

with V_{ech} the sample volume [m^3]. The initialization of the previous equation

for $t = 0$ is made by using the initial laboratory porosity ϕ_L while the final value at the end of the experiment is labeled ϕ_{ch}.

After dissolution, in order to estimate the impact of the experiments on the rock properties, the same laboratory and imaging characterization as before the experiments is conducted on the samples (Section 2.1). To this purpose, centrifugation is conducted in the direction of the pressure difference and in the opposite one, which allows to characterize a possible anisotropy in pore size distribution.

3. Results

3.1. Hydro-chemical results from percolation experiments

Chemical data obtained over time for all the percolation experiments are displayed in Figure 3. In a general way, we observe that the outlet pH values (pH_{out}), fluid conductivities (σ_f) and Ca and Mg concentrations ([Ca] and [Mg]) are higher than the inlet values. The increase in these values indicates that calcite and dolomite dissolution is occurring during the experiments. The curve shapes are globally the same for each parameter, with a first point corresponding to the mixing between water at equilibrium with rock and acidic fluid, a plateau reached when the dissolution begins and then a decrease more or less pronounced at different times depending on the samples. We observe that the decrease in the parameters occurs much sooner for the samples from Normandie than for the samples from Euville and Lexos, whatever the Péclet condition applied.

Even if the curves shape are similar, several observations can be done. The values reached on the plateau for pH, conductivity and Ca and Mg concentrations depend on the rock types and on the Péclet number applied.

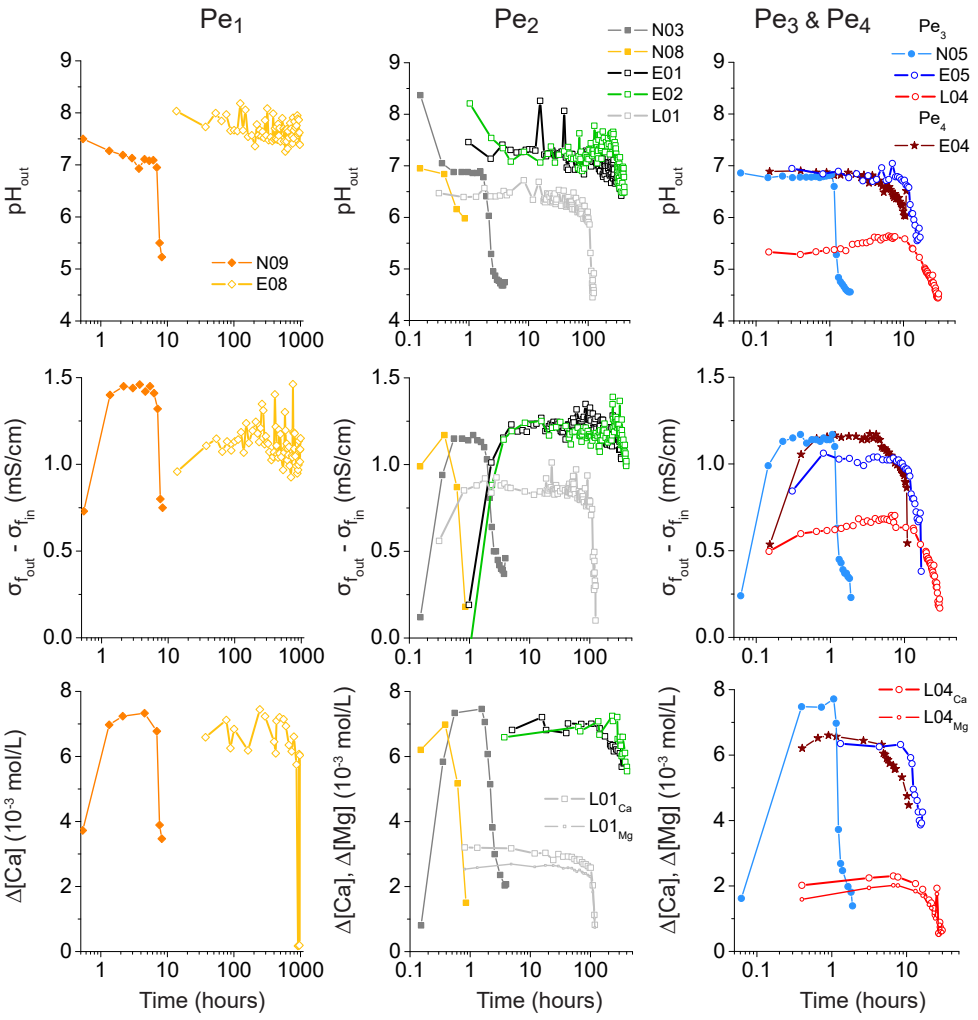

Figure 3: Evolution of the pH at the outlet of the experiments (pH_{out}, first row), the differences in fluid conductivity (σ_f, second row) and calcium and magnesium concentrations between the outlet and inlet of the percolating experiments (Δ[Ca] and Δ[Mg], third row), with Péclet numbers $Pe_1 = 0.09$ (first column, diamonds), $Pe_2 = 0.65$ (second column, squares), $Pe_3 = 1.97$ (third column, circles) and $Pe_4 = 5.26$ (third column, stars). Samples labels with N stand for Normandie chalk, E for Euville crinoidal limestone and L for Lexos dolomite.

Firstly, for each rock type, the plateau values reached for pH and conductivity are independent from the Péclet condition applied. They are similar

for each sample from Normandie and Euville, as they are all considered to be REV. However, we observe a change in the plateau value for Lexos because of the high heterogeneity initially located in $L04_{Pe_3}$. Concerning outlet ions concentrations, samples from Normandie display similar values on the plateau regardless of the Péclet number applied to them, while the plateau values for Euville and Lexos samples decrease with the increase in Pe. Secondly, whatever the Pe is, fluid conductivity and ions concentration obtained for dolomite samples (Lexos) are always lower than the ones of full calcite samples (Normandie and Euville). Concerning Pe_3, the outlet pH of $L04_{Pe_3}$ is lower of 1.5 than the one of $N05_{Pe_3}$ and $E05_{Pe_3}$, whereas the conductivity difference is twice lower. The difference is less pronounced for Pe_2, where $L01_{Pe_2}$ displays a plateau of pH_{out} lower of 0.5 than Normandie and lower of 1 than Euville, and a plateau of conductivity lower of 1 than Normandie and Euville ones. The lower values of pH_{out} in Lexos experiments are due to the smaller quantity of dolomite molecules dissolved compared to calcite ones. Even if the dissolution of one mole of dolomite consumes two times more H^+ than one mole of calcite, limestone samples (Normandie and Euville) display more than twice Ca concentration than dolomite samples. Additionally, we observe that the ratio between Ca and Mg is almost constant during the two experiments for Lexos samples and established to be representative of a stoichiometric dissolution. The corresponding formula is then used for mass balance calculation as explained in Section 2.3.

As explained in Section 2.3, permeability evolution over time during the percolation experiments is calculated from the differential pressure monitoring, and is displayed in Figure 4. We observe an increase in permeability

when we previously observed a decrease in ion concentrations in the effluent. As previously mentioned and explained in Leger et al. (2022), some decreases in permeability can be noticed during the experiments, and are probably due to pores clogging and particles dragging inside the samples (Noiriel et al., 2005; Luquot et al., 2014; Garing et al., 2015).

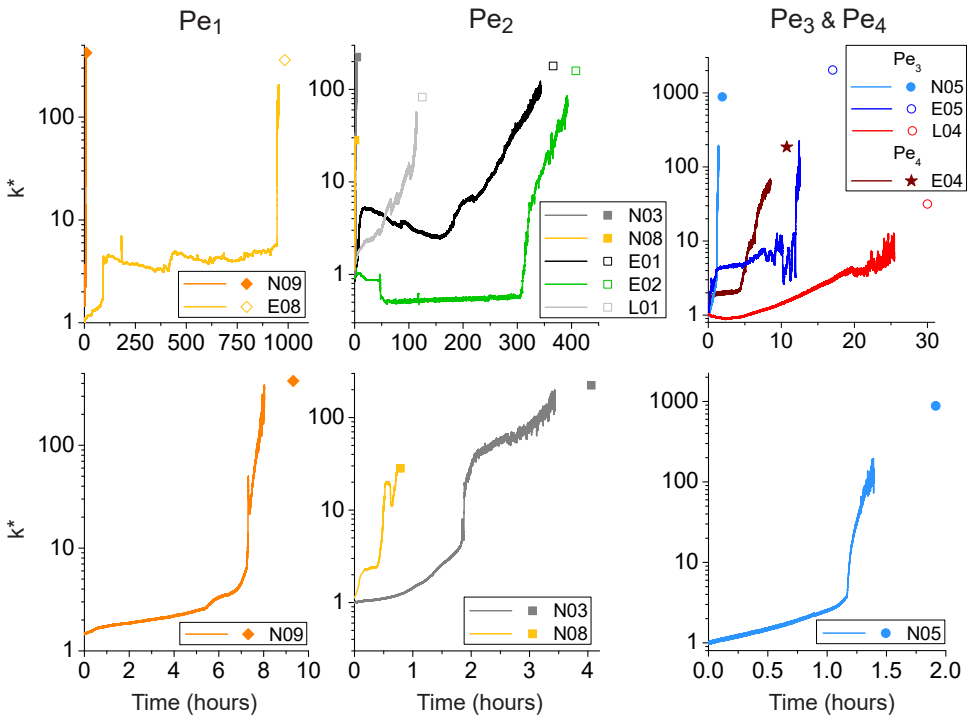

Figure 4: Evolution of the normalized rock permeability k^* [-] during the percolating experiments, where k^* is defined as the permeability of the sample along the experiment normalized by its initial permeability. The dot represents the final value of permeability. Graphics are displayed according to Péclet numbers, in columns (Pe_1, Pe_2 and Pe_3&Pe_4). Due to the large differences in experiments duration, a zoom of Normandie values is displayed on the second row.

Depending on the Pe applied to the samples, the normalized permeability (k^*) evolves in different ways. An important and sudden increase in permeability occurs at different times depending on the samples, and is due to

the percolation inside the core, already defined in previous studies (Daccord, 1987; Fredd and Fogler, 1998; Golfier et al., 2002; Brosse et al., 2005; Luquot and Gouze, 2009; Szymczak and Ladd, 2009; Guarracino et al., 2014; Vialle et al., 2014; Menke et al., 2016; Akono et al., 2019). For Normandie and Euville samples, this sharp increase is followed by a more moderate one, less visible for samples submitted to Pe_1. However, permeability of Lexos samples increases gradually during the experiments. Concerning the importance of the increase in permeability, it is not linear with the Péclet numbers applied to the samples. Indeed, $N08_{Pe_2}$ and $L04_{Pe_3}$ display both the lowest k^* increase, with an increase of only 28 of their permeability. $N05_{Pe_3}$ and $E05_{Pe_3}$ present the highest final relative permeability, with 879 and 2035, respectively. Concerning the other samples, those with Pe_2 display all similar final k^* between 100 and 200 ; whereas $N09_{Pe_1}$ and $E08_{Pe_1}$ both increase their permeability of about 400. Finally, $E04_{Pe_4}$ displays an increase of 186.

3.2. Effective petrophysical and hydraulic parameters

In this section, a focus is made on the petrophysical and hydraulic properties obtained from laboratory measurements and 3D X-ray tomographic images before and after the percolation experiments. These results are displayed in Table 2 and Table 4. The sample $E01_{Pe_2}$ from Euville rock type was not imaged before, so it is not discussed in this part.

Results presented in Table 2 firstly show that the initial properties differ between each rock type. Indeed, Normandie samples are the most porous ones and Euville are the least. Euville samples have the highest formation factors F_L & F_{XR} and tortuosities τ_e & τ_h, while Normandie samples have the lowest, and Lexos samples have parameter values situated between them.

However, permeabilities and cementation indexes are relatively similar for the three rock types. More results on initial rock properties and discussion are available in Leger and Luquot (2021) and in Supplementary Material.

The final porosities of each sample are obtained from laboratory measurements (ϕ_L), microtomographic images ϕ_{XR} and are also calculated from Ca and Mg concentrations with Equation (3) (ϕ_{ch}). The dissolution experiments of the three rock types are not responsible for a significant change in porosity, especially in ϕ_L where some porosity variations are so tiny that they are included in the error measurement, while permeability k_L and k_{XR} increase. Other structural parameters (i.e., formation factor F_L & F_{XR} and tortuosity τ_e & τ_h), calculated from electrical measurements and X-ray images, decrease.

	Samples	Péclet	ϕ_L	ϕ_{XR}		k_L	k_{XR}	F_L	F_{XR}	τ_e	τ_h
Initial	N09	Pe_1	27.2	9.1		0.71	65.2	24.2	31.3	2.57	1.68
	N03	Pe_2	38.0	8.3		11.19	12.6	8.3	36.2	1.78	1.74
	N08	Pe_2	28.8	9.7		8.14	505	26.6	28.8	2.77	1.67
	N05	Pe_3	37.8	7.9		9.07	25.5	7.8	34.1	1.72	1.64
	E08	Pe_1	12.6	5.6		0.06	5.4	178.6	140.6	4.75	2.80
	E01	Pe_2	13.2	-		0.28	-	116.2	-	3.91	-
	E02	Pe_2	14.8	8.0		0.44	10.9	101.0	71.6	3.87	2.40
	E05	Pe_3	12.8	5.9		1.47	24.8	222.2	95.6	5.34	2.38
	E04	Pe_4	14.6	7.2		3.77	112.2	103.1	65.1	3.87	2.17
	L01	Pe_2	18.2	7.4		1.82	1.1	49.0	102.1	2.99	2.74
	L04	Pe_3	18.8	4.7		11.61	10.8	68.5	47.1	3.59	1.48
	Samples	Pe	ϕ_L	ϕ_{XR}	ϕ_{ch}	k_L	k_{XR}	F_L	F_{XR}	τ_e	τ_h
Final	N09	Pe_1	27.2	10.0	27.4	300	1291	15.0	27.3	2.08	1.65
	N03	Pe_2	35.7	8.9	38.3	2500	8059	5.2	24.7	1.36	1.48
	N08	Pe_2	29.7	10.4	28.8	230	1497	11.7	25.5	2.03	1.63
	N05	Pe_3	36.5	8.8	38.2	8000	11304	5.2	26.6	1.38	1.53
	E08	Pe_1	12.9	6.6	13.5	20	28	105.3	87.8	3.68	2.41
	E01	Pe_2	14.7	8.2	15.0	50	18231	29.0	56.1	2.06	2.14
	E02	Pe_2	16.3	9.8	16.9	70	2092	26.1	39.8	2.06	1.98
	E05	Pe_3	12.8	7.1	13.2	3000	7481	50.3	57.0	2.53	2.01
	E04	Pe_4	14.8	7.8	15.1	700	5502	41.5	52.6	2.48	2.03
	L01	Pe_2	20.6	8.9	21.0	150	229550	13.7	23.1	1.68	1.44
	L04	Pe_3	19.3	5.6	20.0	320	5556	25.3	35.5	2.21	1.41

Table 2: Petrophysical properties of samples at initial and final states, i.e., before and after the percolation experiments, from laboratory measurements (porosity ϕ_L [%], permeability k_L [mD], formation factor F_L [-], electrical tortuosity τ_e [-]) and 3D X-ray imaging calculations (porosity ϕ_{XR} [%], permeability k_{XR} [mD], formation factor F_{XR} [-], electrical tortuosity τ_h [-]). The index L stands for Laboratory measurements, XR for X Ray tomographic images and ϕ_{ch} is the porosity from chemistry calculations. The sample E01 was not imaged before experiments. For each rock type, the samples are ordered according to increasing Péclet values.

Each rock type does not react in the same way to percolation experiments. Firstly, concerning Normandie, two groups of samples can be defined. $N03_{Pe_2}$ and $N05_{Pe_3}$ samples both increase the most their permeability and decrease the most their structural properties, contrary to $N08_{Pe_2}$ and $N09_{Pe_1}$ samples. Therefore, $N03_{Pe_2}$ and $N05_{Pe_3}$ samples begin with the lowest permeability to finally reach the highest. Their high decrease in formation factor and tortuosity leads to similar final values between all the samples. $N08_{Pe_2}$ is the sample with the lowest increase in permeability, while it displays the highest decrease in formation factor and tortuosity. A full description of this rock type can be found in Leger et al. (2022).

Secondly, for Euville rock, the samples $E01_{Pe_2}$ and $E02_{Pe_2}$ display the highest increase in porosity, whereas the increase in permeability is the lowest. They also display the highest decrease in formation factors and tortuosities. $E05_{Pe_3}$ is the sample which increases the most its permeability. However, $E08_{Pe_1}$ stays the one with the lowest permeability, before and after the experiment. With the highest step in permeability, the sample $E05_{Pe_3}$ also presents the highest decrease in structural properties, starting with higher values than the other samples and finishing with similar values than all, except $E08_{Pe_1}$. Formation factors and tortuosity values do not decrease much for this latter, which displays the highest final values of structural properties.

Finally, the Lexos set is only composed by two samples. Before the percolation experiments, $L04_{Pe_3}$ has higher initial permeability, formation factor F_L and tortuosity τ_e. The experiments lead to a higher increase in porosity and permeability for the sample $L01_{Pe_2}$, along with a higher decrease in structural factors (F_L & F_{XR} and τ_e & τ_h).

3.3. Pore size and dissolution shape

3.3.1. Pore diameter distribution

For each rock type, pore diameter distributions are obtained before and after the experiments by centrifugation method, and the results are displayed in Figure 5. A distribution is obtained in both drainage directions with slightly different diameter classes depending on the rock type. For Normandie samples, a strong anisotropy is observed after the dissolution experiments, discussed in Leger et al. (2022), and we concluded that the drainage in the opposite direction of dissolution flow is the most representative of the pore size distribution. Euville and Lexos samples do not present as much anisotropy as Normandie samples, and therefore, only distributions obtained from the opposite drainage direction are shown in Figure 5.

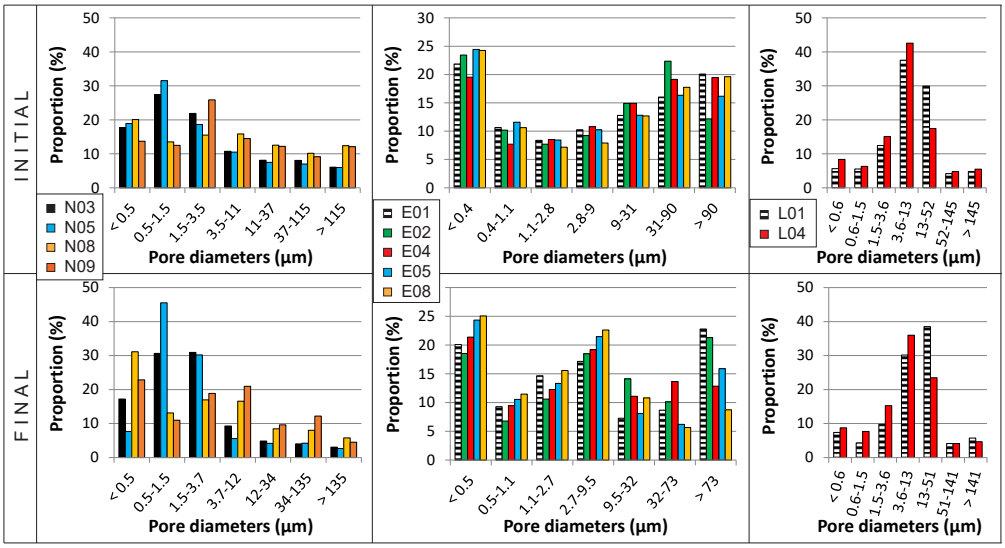

Figure 5: Pore diameters distribution for each sample in each rock type from centrifugation measurements. The Péclet conditions applied to the samples are: Pe_1 (N09, E08), Pe_2 (N03, N08, E01, E02, L01), Pe_3 (N05, E05, L04) and Pe_4 (E04).

In a general way, we observe that the changes in the pore diameters dis-

tributions before and after the percolation experiments are dependent on the rock type. Indeed, samples from Normandie and Euville show a large increase in their proportion of micropores (pores smaller than the XR pixel size equal to 12 μm) with a decrease in large pores proportion. On the opposite, the two samples from Lexos display only few changes between before and after dissolution with a relatively small decrease in micropores proportion, leading to a small increase in macropores proportion. More specifically, concerning Normandie, the evolution depends on the samples. $N03_{Pe_2}$ and $N05_{Pe_3}$ samples display an increase in pores with sizes between 0.5 and 3.7 μm, while a decrease in all the other classes is observed. However, $N08_{Pe_2}$ and $N09_{Pe_1}$ samples show a global increase in all the small pore diameters classes. All the samples from Euville rock display similar trends in the evolution of small pores. The proportion of very small pores (smaller than 0.5 μm) globally remains the same, and the proportion of pores with sizes between 0.5 and 9.5 μm increases. Then, the proportion of large pores decreases for the majority of the samples with more pores larger than 73 μm in $E01_{Pe_2}$ and $E02_{Pe_2}$ than in the other samples.

3.3.2. Pore size distribution and orientation

The homemade software allows to extract the chord length probability distribution of each sample from the 3D images. The equivalent pore size distributions from these calculations are displayed in Figure 6. On one hand, we observe that the pore size globally increases with the experiments, the quantity of small pores (below 24 μm) decreasing and the quantity of large pores (over 100 μm) increasing. On the other hand, the three rock types show different behaviors, before and after experiments, and samples of each

rock type also display differences.

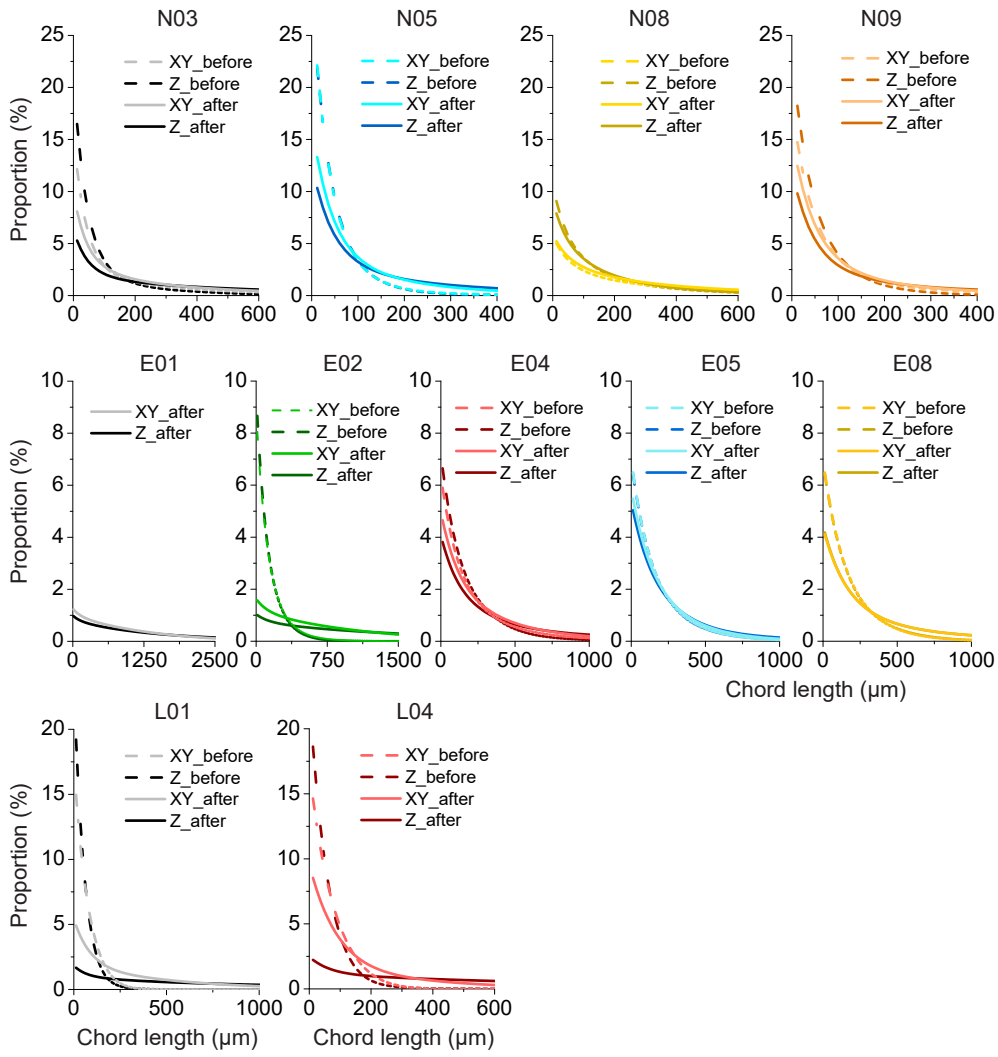

Figure 6: Chord lengths distribution for each sample before (dotted lines) and after (solid lines) percolation. Lines with light colors are for average lengths along X and Y axes, while lines with dark colors are for chord lengths along Z axis. Normandie, Euville and Lexos samples are located on the first, second and third rows, respectively. The Péclet conditions applied to the samples are: Pe_1 (N09, E08), Pe_2 (N03, N08, E01, E02, L01), Pe_3 (N05, E05, L04) and Pe_4 (E04).

Focusing on the global evolution of pore diameters, Normandie samples

are divided into two groups. $N03_{Pe_2}$ and $N05_{Pe_3}$ change the most with the experiment, dividing by two their quantity of small pores and doubling their quantity of large pores, while $N08_{Pe_2}$ and $N09_{Pe_1}$ barely change. This is the same for Euville samples, where $E02_{Pe_2}$ sample decreases a lot its quantity of small pores compared to the other samples. Conversely, the two samples from Lexos change similarly even if the sample $L04_{Pe_3}$ keeps more small pores after experiment than $L01_{Pe_2}$.

An evolution in the pore shapes is also visible. For the Normandie set, $N05_{Pe_3}$ is the only sample displaying spherical pores before the experiments, the others mostly presenting large pores transverse to the flow direction (XY). The dissolution barely changes $N08_{Pe_2}$ pore shape, while large pores in the other samples get longer along the flow direction (Z). Concerning Euville samples, they all present spherical pores before the experiments. The sample $E08_{Pe_1}$, performed with Pe_1 conditions, keeps this shape. However, for the other samples, the large pores enlarge along the flow direction (Z) in different proportion, $E02_{Pe_2}$ displaying the highest difference between the two directions. Lexos samples also have spherical pores before the experiments and display large pores that are larger in the flow direction than in the transverse one after dissolution.

3.3.3. Resulting main flow paths

Micro-tomography images acquisition allows seeing the resulting main flow paths formed during the dissolution experiments (Figure 7). Preferential flow paths created by the acid injections are clearly visible for all the rock types. Initially, these conduits were not present in the cores but some heterogeneities were, as it is shown in Figure 1. A pre-existing filled channel exists

in the central part of $N08_{Pe_2}$, while $N09_{Pe_1}$ displays some micro-cracks. Results for Normandie samples are fully discussed in Leger et al. (2022). $E04_{Pe_4}$ and $E05_{Pe_3}$ both present some zones of initial higher porosity. The first one is composed of two areas, one at the inlet and the other one at the outlet, the acid injection creating a conduit between them, where the rock was more cemented. Inside $E05_{Pe_3}$, the initial higher porosity zone is located on one side (the left one in Figure 7), inducing a preferential dissolution there. The samples $E08_{Pe_1}$ and $L04_{Pe_3}$ both have pre-existing conduits which were not connected to the core sides but help the dissolution process. Additionally, the conduit shapes are different according to the rock type. Dissolution in Normandie chalk samples allows less ramifications than dissolution in Euville crinoidal limestone samples. Indeed, conduits are more linear and precise in the first case. Inside Lexos dolomite samples, dissolution seems to create very linear conduits with few ramifications.

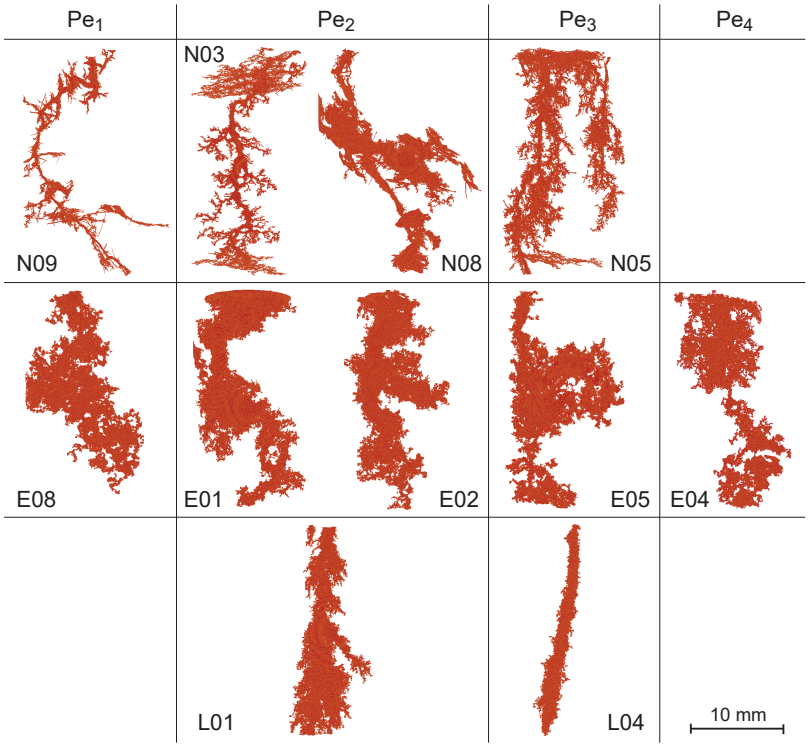

Figure 7: Main path conduits of each sample depending on the four Péclet numbers (in columns) and the rock type (in rows). The samples are all displayed with the acid injection above them. The scale in the bottom right applies to all the samples.

4. Discussion

4.1. Changes in porosity and percolation time

The results presented in Section 3 show that the percolation experiments induce an increase in porosity (ϕ_{ch} from ϕ_L, see Equation (3)) for the three rock types. The evolution of porosity is calculated from outlet cations concentrations (only Ca or both Ca and Mg depending on the rock type) and is displayed in Figure 8. Porosity does not change in the same way depending on the rock type and the Péclet condition of each sample. In a general way, Normandie samples present the lowest increase in porosity, between 0.08 and

0.35%, whereas porosity in Euville samples increases between 0.39 and 2.06% and porosity in Lexos between 1.28 and 2.84% (Figure 8).

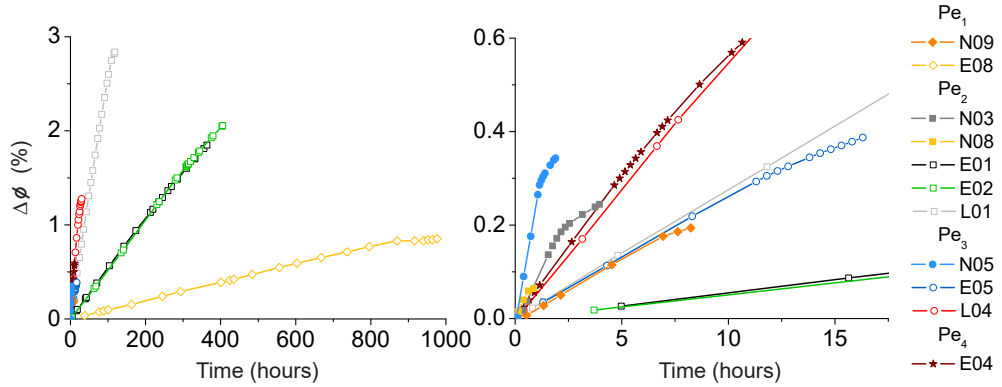

Figure 8: Evolution of rock porosity change, $\Delta\phi$, defined as the porosity measured at time t minus the initial porosity measured in laboratory $\Delta\phi(t) = \phi(t) - \phi_L$ evaluated from Ca and Mg ions concentrations analyzed in the outlet fluid during percolating experiments and using Equation (3). The graph on the right is a zoom of the graph on the left.

As observed in Section 3.1, a break in the porosity curves occurs at different times for each sample (Figure 8). It is more or less pronounced depending on the samples and it defines the percolation time t_p. The corresponding values for each sample are noted in Table 3. For each rock type, we observe in Figure 8 that the higher the Péclet condition applied to the samples, the faster the break in the curves happens and percolation occurs, inducing a lower t_p. The sample N08$_{Pe_2}$ is an exception here due to an important initial heterogeneity, and explanations about this are discussed in Leger et al. (2022). Additionally, concerning rock types only composed of calcite, chalk (Normandie) having a higher initial porosity than crinoidal limestone (Euville), its initial poral volume is higher. To create a conduit, the quantity of rock needed to be dissolved is then less important, inducing a lower increase

in its absolute porosity.

Samples	Pe	t_p	R	R'
N09	Pe_1	7.3	5.86e-9	7.33
N03	Pe_2	1.9	5.17e-8	7.39
N08	Pe_2	0.45	4.49e-8	6.41
N05	Pe_3	1.2	1.31e-7	7.49
E08	Pe_1	893	6.26e-10	6.73
E01	Pe_2	160	3.41e-9	6.82
E02	Pe_2	309	3.45e-9	6.90
E05	Pe_3	11.9	1.58e-8	6.32
E04	Pe_4	4.4	3.86e-8	6.49
L01	Pe_2	105	8.75e-9	2.76
L04	Pe_3	7.7	1.65e-8	2.17

Table 3: Table of experimental properties of each sample. Pe is the Péclet condition applied, R the dissolution rate per acid injection time [mol/s], R' the dissolution rate per acid injection volume [mol/m^3] and t_p is the percolation time [h].

Inside each rock type, the absolute increase in porosity shown in Figure 8 does not seem correlated with the experimental conditions. For Normandie samples, except N08$_{Pe_2}$, porosity increases more when a higher Péclet is applied. In N08$_{Pe_2}$, we observe a minimal increase of 0.08% while it is dissolved with Pe_2. For Euville, samples dissolved with Pe_2 (E01$_{Pe_2}$ and E02$_{Pe_2}$) display a larger increase in porosity than E08$_{Pe_1}$ that is dissolved with Pe_1. However, these three samples increase their porosity more than samples for which Pe_3 and Pe_4 conditions are applied. For Lexos, L01$_{Pe_2}$ increases more its porosity than L04$_{Pe_3}$. However, when considering each Péclet condition applied, the absolute increase in porosity $\Delta\phi$ is always higher in Lexos samples than Euville samples, which have higher increases than Normandie ones. This result seems inconsistent as dolomite dissolution rate is lower than that of calcite (up to one order of magnitude) in similar conditions (Chou et al.,

1989; Gautelier et al., 1999; Morse and Arvidson, 2002; Liu et al., 2005; Pokrovsky et al., 2005). Indeed, in Figure 3, we observe that the outlet Ca concentration for Lexos samples is between one half and one third of Euville samples. This apparent higher porosity increase for Lexos samples than for limestone samples in similar conditions is linked to two different properties. The first one is the mineral molar volume that is higher for the dolomite than for calcite with 64.3 cm^3/mol and 37 cm^3/mol, respectively. The dissolved volume corresponding to one molecule of dolomite is then higher than calcite. The porosity increase in dolomite sample is thus higher than in limestone sample for a same quantity of dissolved mineral. The second important property is the flow rate. In fact, for a similar Pe number, the imposed constant flow rate is different from one rock type to another due to the differences in pore size distribution. Consequently, flow rates applied to dolomite (Lexos) samples are higher than flow rates applied to calcite (Euville) samples (Table 1).

4.2. Impact of the hydraulic conditions and mineral composition on the dissolution rates

Applying higher flow rates for Lexos samples than for Euville samples, in similar Péclet conditions, induces a larger acid renewal inside dolomite samples. It leads to a higher dissolution rate, which is defined as $R = [\mathrm{Ca}] \times Q$ and expressed in mol/s, and related to a higher increase in the porosity that is previously described. Indeed, the slope of the increase in this porosity is directly related to the dissolution rate R, standing between 10^{-10} and 10^{-7} mol/s, depending on the sample (Table 3). This is consistent with existing studies, where for experiments realized in Pe_2 conditions, R is

about 5×10^{-8} mol/s in Noiriel et al. (2009) and 2×10^{-8} mol/s in Luquot et al. (2014); whereas experiments realized with higher Pe lead to R about 8×10^{-7} mol/s (Vialle et al., 2014). Note also that the dissolution rates are similar for the reproductive experiments ($E01_{Pe_2}$-$E02_{Pe_2}$). The slope of the increase in porosity and the dissolution rate R are then both correlated with the Péclet conditions applied to the samples. Indeed, inside each rock type, samples dissolved with lower Pe display lower slopes in Figure 8 and lower R in Table 3. At the same time, when considering each Péclet condition, samples from Normandie always have higher porosity slopes and R than samples from Lexos, which are higher than Euville samples.

For identical Pe numbers, different flow rates are used depending on the rock pore diameters. Therefore, conversely, for two different Pe numbers, a similar flow rate could be applied. Indeed, relatively similar flow rates are applied to $N03_{Pe_2}$, $E04_{Pe_4}$ and $L04_{Pe_3}$, dissolved with Pe_2, Pe_4 and Pe_3, respectively. $N03_{Pe_2}$ displays a dissolution rate 1.3 times higher than $E04_{Pe_4}$, which is 2.3 times higher than $L04_{Pe_3}$. The rate between the quantity of dissolved calcite and the quantity of injected acid is calculated as $R' = \frac{R}{Q}$, and is displayed in Table 3. Lexos samples rates R' are three times lower than Normandie and Euville ones. Therefore, dolomite dissolution is much smaller than calcite one for similar quantity of injected acid. Concerning only samples fully composed of calcite, chalk displays similar but a bit higher R' than crinoidal limestone, which can be explained by a higher reactive surface area in Normandie samples characterized by a higher quantity of small grains.

4.3. Link between the initial rock structure and dissolution rate

Inside each rock type, we observe that the higher the Péclet number applied to the sample, the higher the dissolution rate. In these conditions, the sample $N05_{Pe_3}$ has the highest R while $E08_{Pe_1}$ has the lowest. We observe that some samples from different rock types display similar values of R while they are submitted to different Péclet conditions, such as $N09_{Pe_1}$ with $E01_{Pe_2}$ and $E02_{Pe_2}$, or $E04_{Pe_4}$ with $N03_{Pe_2}$ and $N08_{Pe_2}$. In order to see the impact of the initial rock structure and the experimental conditions on the dissolution rate, Figure 9 displays the dissolution rate R of each sample depending on the initial formation factor F_L and the Pe applied during the corresponding experiment.

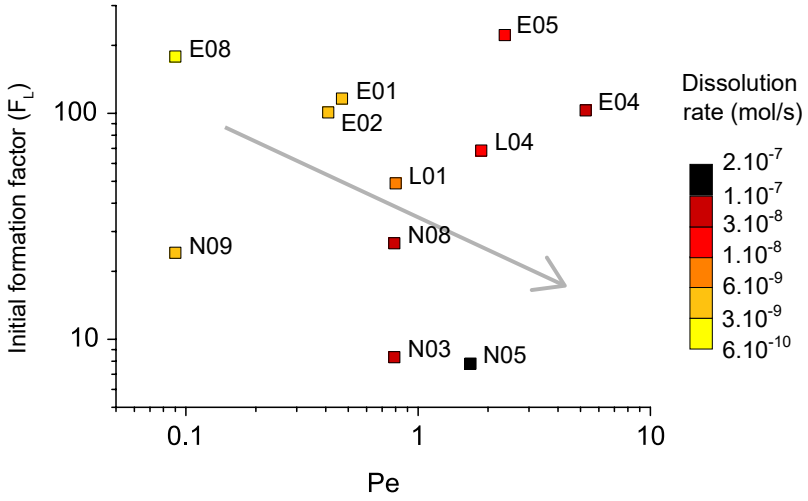

Figure 9: Dissolution rate of each sample, depending on the initial formation factor F_L and the Péclet number Pe applied during the experiments. The color scale shows darker colors for higher dissolution rates R.

Firstly, the higher the Péclet number, the darker the dots representing the samples in Figure 9, showing again that when the acid is injected with high Péclet conditions, the dissolution rate is higher inside the sample. Secondly,

samples from Normandie are situated on the bottom of the graph, while Euville samples are situated on the top and Lexos samples in between. This is due to the difference in formation factors, Normandie having the lowest and Euville the highest. We observe that the lower the formation factor, the darker the dots. The formation factor being defined as the ratio between the electrical conductivity of the fluid and that of the rock sample, it depends on the porosity that is accessible to the fluid and on the heterogeneities of the paths followed by the fluid. Small formation factors are for example associated to fractured rocks where the renewal rate is higher than in porous rocks (Schön, 2015; Roubinet et al., 2018). The higher renewal rate is directly linked to a higher dissolution rate. Here, Normandie samples display the lowest formation factors and highest dissolution rates. Therefore, chalk seems to be a more heterogeneous carbonate rock than crinoidal limestone and dolomite, probably due to its very high proportion of small pores associated to its higher porosity, leading to a lower cohesion compared to the two other rock types.

We observed in Section 3.3.2 that the experimental conditions do not seem to deeply affect the evolution of pore shape inside chalk (Normandie) and dolomite (Lexos) samples (Figure 6). However, concerning crinoidal limestone (Euville), a strong difference exists between $E01_{Pe_2}$ and $E02_{Pe_2}$ and the other samples of the set. After the experiments, the quantity of small pores sharply decreases and the quantity of large pores increases. A link can be established between the quantity of acid injected into the samples during the experiments and the evolution of pore shape. Indeed, even if the percolation experiment in $E08_{Pe_1}$ lasts longer than experiments in $E01_{Pe_2}$

and $E02_{Pe_2}$, the difference in flow rates between the experiments leads to a higher total quantity of acid injected inside $E01_{Pe_2}$ and $E02_{Pe_2}$ than in $E08_{Pe_1}$. Therefore, the total quantity of acid injected into a sample has more impact than the time during which the acid is injected. A very high quantity of acid is then responsible of strong changes in pore shape inside crinoidal limestone. Consequently, it seems that neither the flow condition nor the petrophysical properties changes are the main parameters controlling the reaction but that it is the amount of injected acid and the initial rock properties.

Finally, the conduits shapes displayed in Figure 7 show that dolomite samples are dissolved by creating very linear conduits with few ramifications. This conduit formation explains the linear increase in permeability during the experiments done on Lexos samples. These two observations can be related to the low dissolution kinetic of dolomite compared to calcite. Indeed, the very low rate R' calculated in these samples means a very low quantity of rock dissolved per quantity of injected acid and induces a more localized dissolution than in limestone samples, showing again the strong impact of the initial rock properties on the dissolution process.

5. Conclusions

This study investigates the impact of mineralogy differences on the dissolution of carbonate rock through percolation experiments in similar conditions conducted on samples from three different carbonate rock type: chalk, crinoidal limestone and dolomite. At first, we demonstrated that inside each rock type, the lower the Péclet condition applied to the samples, the lower the dissolution rate. Looking at each Péclet condition, chalk samples display

the highest dissolution rates whereas crinoidal limestone samples display the lowest, and dolomite ones stand in between. Secondly, we highlight that the dolomite dissolution rate is much smaller than the calcite one for similar quantities of acid injected into the samples. This is correlated with a lower dissolution kinetic, inducing localized linear conduits associated with a linear increase in permeability during dissolution experiments.

Then, inside full calcite rock type, the chalk has a larger reactive surface area due to its higher quantity of small grains and it displays slightly higher dissolution rates than crinoidal limestone for similar quantity of acid injected. For a similar quantity of injected acid during the experiments, the flow rate injected is higher in Normandie chalk and induces a higher renewal rate and a lower formation factor.

Finally, for all rock types studied, the dissolution rate seems to be mainly linked to the mineral composition and the acid flow rate, as well as the amount of injected acid in the case of crinoidal limestone. The initial structure of the rock also plays an important role, as we observed that strong heterogeneities and structural parameters affect the dissolution rate and porosity increase.

Supplementary

Materials and methods

Laboratory measurements

The liquid porosity (ϕ_L) and permeability (k_L) of the rock samples are measured by double-weighing saturated and oven-dried samples and from an experimental device applied to saturated samples, respectively. The electrical impedance is defined by injecting electric current in the saturated samples and used to define the rock conductivity, formation factor (F_L), cementation index (m_L) and electrical tortuosity (τ_e) from the well-known equations provided in Waxman and Smits (1968); Archie (1942); Clennell (1997). The P and S waves velocities (Vp and Vs) are obtained by injecting ultrasonic frequency waves of 500 kHz with two piezoelectrical transducers. The pore size distribution is obtained by centrifugation. Following the method described by Reatto et al. (2008); Rötting et al. (2015), increasing velocities are applied on saturated samples. After each cycle of velocity, the water loss is determined by weighing the samples, providing the proportion of a given range of pores size from Young-Laplace equation. Using velocities from 32 to 471 rad/s leads here to pores sizes ranging from approximately 100 to 0.5 µm.

X-ray micro-tomography

3D X-ray micro-tomography (XRMT) images are obtained using the X-ray Computed Tomography (XRCT) scanner (EasyTom 150) of the Institute of Evolution Sciences of Montpellier (ISEM, Montpellier, France) with a pixel size of 12 µm. A homemade imaging software (Gouze et al., 2008) is used to treat the images with filters to improve images quality by smoothing the

pixels histogram and correcting brightness. The two-phase segmentation is done with a region growing method resulting in the macropore and matrix phase, the former corresponding to pores larger than the pixel size and giving the macropore porosity ϕ_{XR}. The sample skeleton is defined as the paths connecting the center of each connected pore and is used to compute the permeability (k_{XR}), hydraulic tortuosity (τ_h), formation factor (F_{XR}) and cementation index (m_{XR}) (Kozeny, 1927; Clennell, 1997; Ghanbarian et al., 2013). The software also provides the pore volume and surface, giving the surface-volume ratio ($\frac{S}{V}$), the pore size distribution with the chord length method (Torquato and Lu, 1993) and the proportion of the percolating phase into the volume sample (PV) from statistics calculations.

Petrophysical properties changes

In this section, we present supplementary data of petrophysical properties that we do not discussed in the main manuscript. In particular, cementation index m_L and m_{XR}, P and S waves velocities, relative pore size $\frac{S}{V}$ and the proportion of the percolating volume from the full porosity PV are presented in Table 4.

Mechanical factors (Vp and Vs velocities) are globally larger for Euville and Lexos samples than for Normandie ones. For the Normandie set, $\mathrm{N08}_{Pe_2}$ is the sample with the highest increase in P and S waves velocity. $\mathrm{N03}_{Pe_2}$ and $\mathrm{N05}_{Pe_3}$ both present the lowest increase in Vp. A full description of this rock type can be found in Leger et al. (2022).

Both $\mathrm{E05}_{Pe_3}$ and $\mathrm{E08}_{Pe_1}$ show a smaller increase in Vp than the other samples. A particularity occurs with the sample $\mathrm{E05}_{Pe_3}$, which is the only one with a decreasing Vs over the dissolution.

Finally, both lexos samples present similar values of P waves velocity and cementation index m_L. However, L04$_{Pe_3}$ has a smaller initial S wave velocity. The sample L04$_{Pe_3}$ displays the highest increase in Vp. The two samples differ in Vs evolution, which decreases for the sample L01$_{Pe_2}$ and increases for the sample L04$_{Pe_3}$.

For all the rock types, structural properties (m_{XR}) and surface ratio ($\frac{S}{V}$) generally decrease, except for m_{XR} of N09$_{Pe_1}$ for which we observe no significant changes. No significant changes are also observed for the percolating volume (PV) for Normandie and Euville samples, while Lexos samples show an important increase.

$\frac{S}{V}$ is lower for Euville than Lexos and then Normandie. Percolating volumes are higher than 93% for all Euville samples, while they stand from 84.7 to 95.9% for Normandie samples, and are below or equal to 68.3% for Lexos samples.

Every sample of each rock type does not change in the same way with dissolution. Concerning Normandie, two groups of samples can be defined. N03$_{Pe_2}$ and N05$_{Pe_3}$ samples both decrease the most their structural properties and surface ratio, contrary to N08$_{Pe_2}$ and N09$_{Pe_1}$ samples. However, final $\frac{S}{V}$ values are about 100 mm^{-1} for the samples N03$_{Pe_2}$, N05$_{Pe_3}$ and N09$_{Pe_1}$, while it equals 85 mm^{-1} for the sample N08$_{Pe_2}$. For Euville rock type, E02$_{Pe_2}$ displays the highest decrease in m_{XR} and $\frac{S}{V}$, on the contrary to E04$_{Pe_4}$. For Lexos rock type, the properties of the sample L01$_{Pe_2}$ change the most between before and after the experiments. We observe that the dissolution barely affects the cementation index of L04$_{Pe_3}$, while both samples reach similar final values in m_{XR}, $\frac{S}{V}$ and PV. The experiments lead to a higher

643 decrease in structural factors (m_L) for the sample L01$_{Pe_2}$.

	Samples	m_L	m_{XR}	Vp	Vs	$\frac{S}{V}$	PV
Initial	$N09_{Pe_1}$	2.45	1.43	2.97	1.64	103.0	94.9
	$N03_{Pe_2}$	2.19	1.44	2.36	1.18	113.0	84.7
	$N08_{Pe_2}$	2.63	1.44	2.33	1.30	87.6	95.9
	$N05_{Pe_3}$	2.12	1.39	2.35	1.25	111.4	86.1
	$E08_{Pe_1}$	2.51	1.71	3.86	2.10	33.7	93.0
	$E01_{Pe_2}$	2.35	-	3.08	1.90	-	-
	$E02_{Pe_2}$	2.42	1.69	2.32	1.30	41.9	99.1
	$E05_{Pe_3}$	2.63	1.61	3.73	2.04	37.4	98.9
	$E04_{Pe_4}$	2.41	1.59	2.56	1.42	40.8	95.1
	$L01_{Pe_2}$	2.29	1.77	3.40	2.00	68.5	42.1
	$L04_{Pe_3}$	2.53	1.26	3.10	1.86	65.8	68.3
	Samples	m_L	m_{XR}	Vp	Vs	$\frac{S}{V}$	PV
Final	$N09_{Pe_1}$	2.08	1.44	3.89	1.83	98.9	94.8
	$N03_{Pe_2}$	1.60	1.33	2.76	1.65	103.5	86.4
	$N08_{Pe_2}$	2.03	1.43	3.74	2.01	85.0	95.7
	$N05_{Pe_3}$	1.63	1.35	2.80	1.85	100.9	89.1
	$E08_{Pe_1}$	2.27	1.65	5.33	2.18	33.1	92.5
	$E01_{Pe_2}$	1.75	1.61	5.27	2.07	29.8	99.6
	$E02_{Pe_2}$	1.80	1.59	5.08	2.00	34.8	99.5
	$E05_{Pe_3}$	1.90	1.53	5.45	1.81	34.4	96.8
	$E04_{Pe_4}$	1.95	1.56	5.32	1.91	38.2	99.1
	$L01_{Pe_2}$	1.66	1.30	4.74	1.85	57.9	88.3
	$L04_{Pe_3}$	1.96	1.24	4.81	1.94	57.7	88.6

Table 4: Petrophysical properties of samples at initial and final states, i.e., before and after the percolation experiments from laboratory measurements and 3D X-ray imaging calculations with cementation index m_L [-] & m_{XR} [-], and P and S wave velocities Vp and Vs [km/s], ratio of pore surface over pore volume $\frac{S}{V}$ [mm^{-1}] and proportion of percolating volume PV [%]. The index L stands for Laboratory measurements and XR for 3D microtomographic images. The sample E01 was not imaged before experiments. For each rock type, the samples are ordered according to increasing Péclet values.

References

Akono, A., Druhan, J.L., Dávila, G., Tsotsis, T., Jessen, K., Fuchs, S., Crandall, D., Shi, Z., Dalton, L., Tkach, M.K., Goodman, A.L., Frailey, S., Werth, C.J., 2019. A review of geochemical–mechanical impacts in geological carbon storage reservoirs. Greenhouse Gas Sci Technol 9, 474–504. doi:10.1002/ghg.1870.

Archie, G., 1942. The Electrical Resistivity Log as an Aid in Determining Some Reservoir Characteristics. Transactions of the AIME 146, 54–62. doi:10.2118/942054-G.

Brosse, E., Magnier, C., Vincent, B., 2005. Modelling Fluid-Rock Interaction Induced by the Percolation of CO2 -Enriched Solutions in Core Samples: the Role of Reactive Surface Area. Oil & Gas Science and Technology - Rev. IFP 60, 287–305. doi:10.2516/ogst:2005018.

Chilingarian, G.V., Mazzullo, S.J., Rieke, H.H., 1992. Carbonate reservoir characterization: a geologic-engineering analysis. Number 30, 44 in Developments in petroleum science, Elsevier, Amsterdam ; New York, NY, USA.

Choquette, P.W., Pray, L.C., 1970. Geologic Nomenclature and Classification of Porosity in Sedimentary Carbonates. Bulletin 54. doi:10.1306/5D25C98B-16C1-11D7-8645000102C1865D.

Chou, L., Garrels, R.M., Wollast, R., 1989. Comparative study of the kinetics and mechanisms of dissolution of carbonate minerals. Chemical Geology 78, 269–282. doi:10.1016/0009-2541(89)90063-6.

Clennell, M.B., 1997. Tortuosity: a guide through the maze. Geological Society, London, Special Publications 122, 299–344. URL: http://sp.lyellcollection.org/lookup/doi/10.1144/GSL.SP.1997.122.01.18, doi:10.1144/GSL.SP.1997.122.01.18.

Daccord, G., 1987. Chemical dissolution of a porous medium by a reactive fluid. Phys. Rev. Lett. 58, 479–482. doi:10.1103/PhysRevLett.58.479.

Daccord, G., Lenormand, R., Liétard, O., 1993. Chemical dissolution of a porous medium by a reactive fluid—I. Model for the "wormholing" phenomenon. Chemical Engineering Science 48, 169–178. doi:10.1016/0009-2509(93)80293-Y.

Elkhoury, J.E., Ameli, P., Detwiler, R.L., 2013. Dissolution and deformation in fractured carbonates caused by flow of CO2-rich brine under reservoir conditions. International Journal of Greenhouse Gas Control 16, S203–S215. doi:10.1016/j.ijggc.2013.02.023.

Ford, D., Williams, P., 2007. Karst Hydrogeology and Geomorphology: Ford/Karst Hydrogeology and Geomorphology. John Wiley & Sons Ltd,., West Sussex, England. doi:10.1002/9781118684986.

Fredd, C.N., Fogler, H.S., 1998. Influence of transport and reaction on wormhole formation in porous media. AIChE J. 44, 1933–1949. doi:10.1002/aic.690440902.

Garcia-Rios, M., Luquot, L., Soler, J.M., Cama, J., 2017. The role of mineral heterogeneity on the hydrogeochemical response of two fractured reservoir

689 rocks in contact with dissolved CO2. Applied Geochemistry 84, 202–217.
690 doi:10.1016/j.apgeochem.2017.06.008.

691 Garing, C., Gouze, P., Kassab, M., Riva, M., Guadagnini, A., 2015. Anti-
692 correlated Porosity–Permeability Changes During the Dissolution of Car-
693 bonate Rocks: Experimental Evidences and Modeling. Transp Porous Med
694 107, 595–621. doi:10.1007/s11242-015-0456-2.

695 Gautelier, M., Oelkers, E.H., Schott, J., 1999. An experimental study of
696 dolomite dissolution rates as a function of pH from -0.5 to 5 and temper-
697 ature from 25 to 80°C. Chemical Geology 157, 13–26. doi:10.1016/S0009-
698 2541(98)00193-4.

699 Ghanbarian, B., Hunt, A.G., Ewing, R.P., Sahimi, M., 2013. Tortuosity in
700 Porous Media: A Critical Review. Soil Science Society of America Journal
701 77, 1461–1477. URL: http://doi.wiley.com/10.2136/sssaj2012.0435,
702 doi:10.2136/sssaj2012.0435.

703 Gharbi, O., Bijeljic, B., Boek, E., Blunt, M.J., 2013. Changes in Pore
704 Structure and Connectivity Induced by CO2 Injection in Carbonates:
705 A Combined Pore-Scale Approach. Energy Procedia 37, 5367–5378.
706 doi:10.1016/j.egypro.2013.06.455.

707 Golfier, F., Zarcone, C., Bazin, B., Lenormand, R., Lasseux, D., Quintard,
708 M., 2002. On the ability of a Darcy-scale model to capture wormhole
709 formation during the dissolution of a porous medium. Journal of Fluid
710 Mechanics 457. doi:10.1017/S0022112002007735.

Gouze, P., Melean, Y., Le Borgne, T., Dentz, M., Carrera, J., 2008. Non-Fickian dispersion in porous media explained by heterogeneous microscale matrix diffusion. Water Resour. Res. 44. URL: http://doi.wiley.com/10.1029/2007WR006690, doi:10.1029/2007WR006690.

Guarracino, L., Rötting, T., Carrera, J., 2014. A fractal model to describe the evolution of multiphase flow properties during mineral dissolution. Advances in Water Resources 67, 78–86. doi:10.1016/j.advwatres.2014.02.011.

Hoefner, M.L., Fogler, H.S., 1988. Pore evolution and channel formation during flow and reaction in porous media. AIChE J. 34, 45–54. doi:10.1002/aic.690340107.

Kozeny, J., 1927. Uber kapillare Leitung des Wassers im Boden. Sitzungberichte der Akadamie der Wissenschaftung in Wien Abteilung Ila , 271–301.

Lasaga, A.C., 1984. Chemical kinetics of water-rock interactions. J. Geophys. Res. 89, 4009–4025. doi:10.1029/JB089iB06p04009.

Lebedev, M., Zhang, Y., Sarmadivaleh, M., Barifcani, A., Al-Khdheeawi, E., Iglauer, S., 2017. Carbon geosequestration in limestone: Pore-scale dissolution and geomechanical weakening. International Journal of Greenhouse Gas Control 66, 106–119. doi:10.1016/j.ijggc.2017.09.016.

Leger, M., Luquot, L., 2021. Importance of Microstructure in Carbonate Rocks: Laboratory and 3D-Imaging Petrophysical Characterization. Applied Sciences 11, 3784. doi:10.3390/app11093784.

734 Leger, M., Roubinet, D., Jamet, M., Luquot, L., 2022. Impact of hydro-
735 chemical conditions on structural and hydro-mechanical properties of chalk
736 samples during dissolution experiments. Chemical Geology 594, 120763.
737 doi:10.1016/j.chemgeo.2022.120763.

738 Levenson, Y., Schiller, M., Kreisserman, Y., Emmanuel, S., 2015. Calcite
739 dissolution rates in texturally diverse calcareous rocks. Geological Society,
740 London, Special Publications 406, 81–94. doi:10.1144/SP406.14.

741 Liu, Z., Yuan, D., Dreybrodt, W., 2005. Comparative study of dissolution
742 rate-determining mechanisms of limestone and dolomite. Environ Geol 49,
743 274–279. doi:10.1007/s00254-005-0086-z.

744 Lucia, F.J., 1983. Petrophysical parameters estimated from visual descrip-
745 tions of carbonate rocks. Journal of Petroleum Technology, 35, 629–637.

746 Luhmann, A.J., Kong, X.Z., Tutolo, B.M., Garapati, N., Bagley, B.C.,
747 Saar, M.O., Seyfried, W.E., 2014. Experimental dissolution of dolomite
748 by CO2-charged brine at 100°C and 150bar: Evolution of porosity, per-
749 meability, and reactive surface area. Chemical Geology 380, 145–160.
750 doi:10.1016/j.chemgeo.2014.05.001.

751 Luquot, L., Gouze, P., 2009. Experimental determination of porosity and
752 permeability changes induced by injection of CO2 into carbonate rocks.
753 Chemical Geology 265, 148–159. doi:10.1016/j.chemgeo.2009.03.028.

754 Luquot, L., Rodriguez, O., Gouze, P., 2014. Experimental Characterization
755 of Porosity Structure and Transport Property Changes in Limestone Un-
756 dergoing Different Dissolution Regimes. Transp Porous Med 101, 507–

532. URL: http://link.springer.com/10.1007/s11242-013-0257-4, doi:10.1007/s11242-013-0257-4.

Lønøy, A., 2006. Making sense of carbonate pore systems. Bulletin 90, 1381–1405. URL: http://search.datapages.com/data/doi/10.1306/03130605104, doi:10.1306/03130605104.

Mangane, P.O., Gouze, P., Luquot, L., 2013. Permeability impairment of a limestone reservoir triggered by heterogeneous dissolution and particles migration during CO2-rich injection: dissolution-induced particle migration. Geophys. Res. Lett. 40, 4614–4619. doi:10.1002/grl.50595.

de Marsily, G., 1986. Quantitative hydrogeology; groundwater hydrology for engineers. Academic Press .

Menke, H., Andrew, M., Blunt, M., Bijeljic, B., 2016. Reservoir condition imaging of reactive transport in heterogeneous carbonates using fast synchrotron tomography — Effect of initial pore structure and flow conditions. Chemical Geology 428, 15–26. doi:10.1016/j.chemgeo.2016.02.030.

Menke, H., Bijeljic, B., Blunt, M., 2017. Dynamic reservoir-condition microtomography of reactive transport in complex carbonates: Effect of initial pore structure and initial brine pH. Geochimica et Cosmochimica Acta 204, 267–285. doi:10.1016/j.gca.2017.01.053.

Menke, H.P., Bijeljic, B., Andrew, M.G., Blunt, M.J., 2015. Dynamic Three-Dimensional Pore-Scale Imaging of Reaction in a Carbonate at Reservoir Conditions. Environ. Sci. Technol. 49, 4407–4414. doi:10.1021/es505789f.

780 Moore, C.H., Wade, W.J., 2013. Carbonate reservoirs: porosity and diage-
781 nesis in a sequence stratigraphic framework. Number 67 in Developments
782 in sedimentology. second edition ed., Elsevier, Amsterdam.

783 Morse, J.W., Arvidson, R.S., 2002. The dissolution kinetics of ma-
784 jor sedimentary carbonate minerals. Earth-Science Reviews 58, 51–84.
785 doi:10.1016/S0012-8252(01)00083-6.

786 Noiriel, C., Bernard, D., Gouze, P., Thibault, X., 2005. Hydraulic Prop-
787 erties and Microgeometry Evolution Accompanying Limestone Dissolu-
788 tion by Acidic Water. Oil & Gas Science and Technology 60, 177–192.
789 doi:10.2516/ogst:2005011.

790 Noiriel, C., Gouze, P., Bernard, D., 2004. Investigation of porosity and per-
791 meability effects from microstructure changes during limestone dissolution.
792 Geophysical Research Letters 31. doi:10.1029/2004GL021572.

793 Noiriel, C., Luquot, L., Madé, B., Raimbault, L., Gouze, P., van der Lee,
794 J., 2009. Changes in reactive surface area during limestone dissolution:
795 An experimental and modelling study. Chemical Geology 265, 160–170.
796 doi:10.1016/j.chemgeo.2009.01.032.

797 Pokrovsky, O.S., Golubev, S.V., Schott, J., 2005. Dissolution kinetics of
798 calcite, dolomite and magnesite at 25 °C and 0 to 50 atm pCO2. Chemical
799 Geology 217, 239–255. doi:10.1016/j.chemgeo.2004.12.012.

800 Reatto, A., Da Silva, E.M., Bruand, A., Souza Martins, E., Lima, J.E.F.W.,
801 2008. Validity of the Centrifuge Method for Determining the Water Reten-

802 tion Properties of Tropical Soils. Soil Science Society of America Journal
803 72, 1547–1553. doi:10.2136/sssaj2007.0355N.

804 Rege, S.D., Fogler, H.S., 1989. Competition among flow, dissolu-
805 tion, and precipitation in porous media. AIChE J. 35, 1177–1185.
806 doi:10.1002/aic.690350713.

807 Rohmer, J., Pluymakers, A., Renard, F., 2016. Mechano-chemical
808 interactions in sedimentary rocks in the context of CO 2 storage:
809 Weak acid, weak effects? Earth-Science Reviews 157, 86–110.
810 doi:10.1016/j.earscirev.2016.03.009.

811 Roubinet, D., Irving, J., Pezard, P., 2018. Relating Topological and Electrical
812 Properties of Fractured Porous Media: Insights into the Characterization
813 of Rock Fracturing. Minerals 8, 14. doi:10.3390/min8010014.

814 Rötting, T.S., Luquot, L., Carrera, J., Casalinuovo, D.J., 2015. Changes
815 in porosity, permeability, water retention curve and reactive surface area
816 during carbonate rock dissolution. Chemical Geology 403, 86–98. URL:
817 http://www.sciencedirect.com/science/article/pii/S0009254115001424,
818 doi:10.1016/j.chemgeo.2015.03.008.

819 Schön, J., 2015. Physical properties of rocks: fundamentals and principles of
820 petrophysics. Number volume 65 in Developments in petroleum science.
821 2nd edition ed., Elsevier, Amsterdam, Netherlands.

822 Smith, M.M., Sholokhova, Y., Hao, Y., Carroll, S.A., 2013. Evaporite
823 Caprock Integrity: An Experimental Study of Reactive Mineralogy and

824 Pore-Scale Heterogeneity during Brine-CO2 Exposure. Environmental Sci-
825 ence & Technology 47, 262–268. doi:10.1021/es3012723.

826 Steefel, C.I., Beckingham, L.E., Landrot, G., 2015. Micro-Continuum Ap-
827 proaches for Modeling Pore-Scale Geochemical Processes. Reviews in Min-
828 eralogy and Geochemistry 80, 217–246. doi:10.2138/rmg.2015.80.07.

829 Szymczak, P., Ladd, A.J.C., 2009. Wormhole formation in dissolving frac-
830 tures. J. Geophys. Res. 114, B06203. doi:10.1029/2008JB006122.

831 Torquato, S., Lu, B., 1993. Chord-Length Distribution Function for Two-
832 Phase Random Media. Physical Review E 47.

833 Tutolo, B.M., Luhmann, A.J., Kong, X.Z., Saar, M.O., Seyfried, W.E.,
834 2014. Experimental Observation of Permeability Changes In Dolomite
835 at CO2 Sequestration Conditions. Environ. Sci. Technol. 48, 2445–2452.
836 doi:10.1021/es4036946.

837 Vialle, S., Contraires, S., Zinzsner, B., Clavaud, J., Mahiouz, K., Zuddas, P.,
838 Zamora, M., 2014. Percolation of CO2 -rich fluids in a limestone sample:
839 Evolution of hydraulic, electrical, chemical, and structural properties. J.
840 Geophys. Res. Solid Earth 119, 2828–2847. doi:10.1002/2013JB010656.

841 Vialle, S., Dvorkin, J., Mavko, G., 2013. Implications of pore microgeom-
842 etry heterogeneity for the movement and chemical reactivity of CO2 in
843 carbonates. GEOPHYSICS 78, L69–L86. doi:10.1190/geo2012-0458.1.

844 Vialle, S., Vanorio, T., 2011. Laboratory measurements of elastic properties
845 of carbonate rocks during injection of reactive CO2-saturated water: Ef-

fect of CO2-rich water in carbonates. Geophys. Res. Lett. 38, n/a–n/a. doi:10.1029/2010GL045606.

Wang, H., Alvarado, V., Bagdonas, D.A., McLaughlin, J.F., Kaszuba, J.P., Grana, D., Campbell, E., Ng, K., 2021. Effect of CO2-brine-rock reactions on pore architecture and permeability in dolostone: Implications for CO2 storage and EOR. International Journal of Greenhouse Gas Control 107, 103283. doi:10.1016/j.ijggc.2021.103283.

Waxman, M., Smits, L., 1968. Electrical conductivities in oil-bearing shaly sands. Society of Petroleum Engineers Journal 8, 107–122. URL: http://www.onepetro.org/doi/10.2118/1863-A, doi:10.2118/1863-A.